

Aeolian processes in Proctor Crater on Mars: Mesoscale modeling of dune-forming winds

Lori K. Fenton

Department of Geology, Arizona State University, Tempe, Arizona, USA

Anthony D. Toigo

Graduate School of Science and Technology, Kobe University, Kobe, Japan

Mark I. Richardson

Division of Geological and Planetary Sciences, California Institute of Technology, Pasadena, California, USA

Received 23 June 2004; revised 14 March 2005; accepted 11 April 2005; published 16 June 2005.

[1] Both atmospheric modeling and spacecraft imagery of Mars are now of sufficient quality that the two can be used in conjunction to acquire an understanding of regional- and local-scale aeolian processes on Mars. We apply a mesoscale atmospheric model adapted for use on Mars (the Mars MM5) to Proctor Crater, a 150 km diameter crater in the southern highlands. Proctor Crater contains numerous aeolian features that indicate wind direction, including a large dark dune field with reversing transverse and star dunes containing three different slipface orientations, small and older bright bedforms that are most likely transverse granule ripples, and seasonally erased dust devil tracks. Results from model runs spanning a Martian year, with a horizontal grid spacing of 10 km, predict winds aligned with two of the three dune slipfaces as well as spring and summer winds matching the dust devil track orientations. The primary (most prevalent) dune slipface orientation corresponds to a fall and winter westerly wind created by geostrophic forces. The tertiary dune slipface orientation is caused by spring and summer evening katabatic flows down the eastern rim of the crater, influencing only the eastern portion of the crater floor. The dunes are trapped in the crater because the tertiary winds, enhanced by topography, counter transport from the oppositely oriented primary winds, which may have originally carried sand into the crater. The dust devil tracks are caused by light spring and summer westerly winds during the early afternoon caused by planetary rotation. The secondary dune slipface orientation is not predicted by model results from either the Mars MM5 or the Geophysical Fluid Dynamics Laboratory Mars general circulation model. The reason for this is not clear, and the wind circulation pattern that creates this dune slipface is not well constrained. The Mars MM5 model runs do not predict stresses above the saltation threshold for dune sand of the appropriate size and composition. As with previous work, the calculated wind velocities are too low, which may be caused by too large of a grid spacing.

Citation: Fenton, L. K., A. D. Toigo, and M. I. Richardson (2005), Aeolian processes in Proctor Crater on Mars: Mesoscale modeling of dune-forming winds, *J. Geophys. Res.*, 110, E06005, doi:10.1029/2004JE002309.

1. Introduction

1.1. Background

[2] The dominance of wind action over other contemporary surface processes on Mars became evident during the Mariner 9 mission in 1971–1972 [e.g., *McCauley et al.*, 1972; *Sagan et al.*, 1972; *Smith*, 1972; *Cutts and Smith*, 1973; *Arvidson*, 1974]. Wind circulation patterns determine the location and magnitude of sources, sinks, and transport pathways of particulate materials. Because of this coupling

between surface materials and the atmosphere, the study of one is not complete without the study of the other. In particular, dune morphology is dependent on winds that are strong enough to transport sand. Thus a study of dune morphology leads to an understanding of the directions of strong local winds. Furthermore, there are few wind measurements available for use as “ground truth” for atmospheric models. Aeolian features are aligned with the winds that formed them, providing the only indicator of surface wind direction that spans the planet. Thus a comparison of modeled wind predictions with orientations of surface features is one of the few verification techniques available for both the modeled surface winds and the

applied boundary layer scheme. It is the atmospheric counterpart to surficial geology that is discussed in this work.

[3] Shortly after the discovery of sand dunes on Mars, experimental work in wind tunnels began in order to better understand the physics behind sand saltation under Martian atmospheric conditions [Iversen *et al.*, 1973, 1976]. The results indicate that there are many differences in the mechanics of saltation on Mars and Earth. The friction speed u_* is related to the change in horizontal wind velocity as a function of height $u(z)$ by the Prandtl-von Karman equation:

$$u(z) = (u_*/k) \ln(z/z_0), \quad (1)$$

where k is von Karman's constant (~ 0.4 on Earth), z is the height above the ground, and z_0 is the aerodynamic roughness length of the surface. The friction speed is also related to the shear stress at the bed τ and the air density ρ_a by

$$u_* = (\tau/\rho_a)^{1/2}. \quad (2)$$

Above a threshold shear stress τ_t or friction speed u_* , the wind exerts enough stress on the surface to move sand grains into saltation. For further discussion, see discussions by Bagnold [1941] and White [1979]. Greeley *et al.* [1980] found that threshold friction speeds an order of magnitude larger than those measured on the Earth are required to move similarly sized sand grains on Mars (u_* of 0.22 m s^{-1} for Earth versus 2.2 m s^{-1} for Mars). Iversen and White [1982] improved on previous work, producing new empirical relations for threshold friction speeds. They found that saltating particles on Mars would have longer path lengths than those on Earth, and that this parameter varies with temperature and atmospheric conditions. In addition, White [1979] showed that although it takes stronger winds to saltate sand on Mars, once saltation begins, the sand flux on Mars would be significantly higher than that on Earth. Now that sand grain sizes and compositions are being constrained using Thermal Emission Spectrometer (TES) data from the Mars Global Surveyor (MGS), a more precise estimate of saltation threshold stresses may be utilized in detecting sand saltation and calculating sand mass fluxes.

[4] In the last decade, atmospheric models have been applied in conjunction with the results from wind tunnel experiments to better understand aeolian processes on Mars. Greeley *et al.* [1993] used a Mars general circulation model (GCM) to study the correlation of surface wind patterns to aeolian features with measurable wind-aligned orientations. They found that bright depositional streaks correspond well to the southern summer Hadley circulation, but that dark erosional streaks and yardangs did not agree well with any modeled winds above the saltation threshold. Fenton and Richardson [2001] later found that a higher time resolution (hours rather than days) in a Mars GCM resolved the nighttime winds that correlated well with dark erosional streaks, implying that temporal and spatial resolution in models is one of the keys to understanding some of the previously unexplained aeolian features. Yardang orienta-

tions are not aligned with current winds, but some of these features may be so old that they were formed under ancient and unconstrained wind conditions that cannot be properly modeled without further information. Other applications of modeling the Martian surface on a regional or global scale have included finding bimodal (bidirectional) winds in an area where longitudinal dunes indicate such a wind regime should exist [Lee and Thomas, 1995]; locating global sand sources and sinks [Anderson *et al.*, 1999]; and looking for changes in surface wind patterns caused by variations in orbital parameters [Fenton and Richardson, 2001].

[5] With the application of mesoscale atmospheric models to Mars, the circulation of a small region now can be examined at a high spatial resolution. These models can be used in concert with spacecraft data, and in particular MOC NA (Mars Orbiter Camera Narrow Angle) images, which may have aeolian features with wind-aligned orientations at the scale of tens of meters. Comparing the two provides not only a verification of the mesoscale model and the GCM to which it is coupled, but also an understanding of the winds that influence the surface (although care must be taken to ensure that coincidental alignment of modeled winds with observed features is not overinterpreted). This in turn can lead to a better understanding of landscape morphology and the sources and sinks of mobile material. For example, a mesoscale model has been applied over a crater and a valley, demonstrating that topographic and diurnal effects dominate the local windflow on Mars [Greeley *et al.*, 2001]. A mesoscale model applied over the Antarctic ice sheets has been used as an analog to the north polar residual ice cap on Mars in order to explain the presence of most of the surface features [Howard, 2000]. Mesoscale airflow has been modeled over a typical crater to show that the highest wind stresses occur on the downwind crater rim, consistent with erosion patterns observed in small craters [Kuzmin *et al.*, 2001]. Orientations of various aeolian features have been compared to mesoscale modeled winds at both of the Mars Exploration Rover landing sites to provide context for the missions [Greeley and Thompson, 2003; Greeley *et al.*, 2003]. It has become clear that models with both higher spatial and temporal resolution are necessary to understand local and even regional wind patterns.

[6] This work is the second of two papers describing aeolian processes in Proctor Crater, a 150 km diameter crater in the ancient cratered highlands of Noachis Terra (see Figure 1). The first paper, Fenton *et al.* [2003] (hereafter called Paper 1), discusses the morphology, composition, thermal properties, and stratigraphic history of the floor materials within Proctor Crater. With use of a number of different data sets in conjunction, it is shown in Paper 1 that the sedimentary history of Proctor Crater has involved a complex interaction of accumulating and eroding sediments. Aeolian features spanning much of the history of the crater interior dominate its surface, including large erosional pits, hundreds of meters of stratified beds of aeolian sediments, sand dunes, erosional and depositional streaks, dust devil tracks, and small bright bedforms that are probably granule ripples. In this work we apply a mesoscale model to the atmosphere above Proctor Crater in order to determine how modeled winds correspond to the aeolian features described

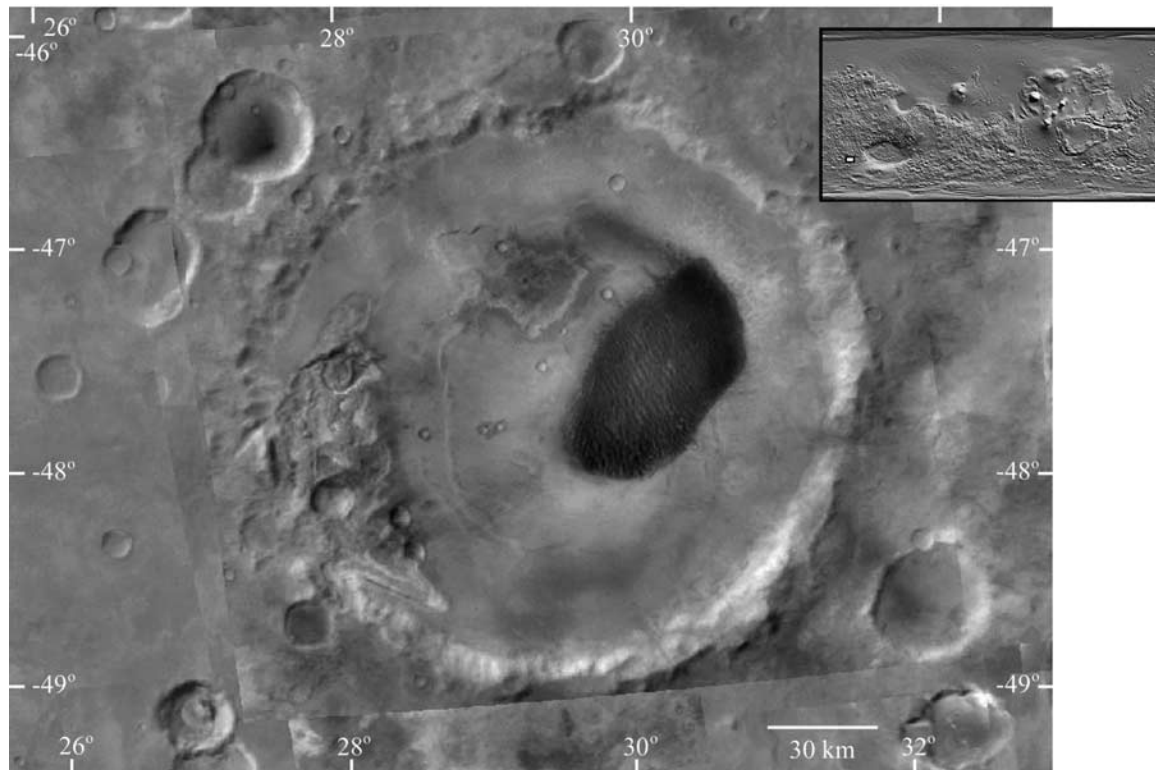


Figure 1. MOC wide-angle mosaic of Proctor Crater, a 150 km diameter crater with an interior dark dune field, located in the southern highlands ~900 km west of Hellas Basin (see inset).

in Paper 1. First we review the orientations of aeolian features found in Paper 1, with an additional discussion regarding evidence for seasonally reversing slipfaces found in MOC NA images. We then describe the mesoscale model and how the resulting wind predictions correlate to known surface features. We discuss seasonal and daily wind changes and the spatial variation of wind patterns on the Proctor Crater floor. Using sand grain density and particle sizes estimated in Paper 1 we discuss the likelihood of sand lifting under the predicted wind conditions.

1.2. Describing Wind Directions and Aeolian Feature Orientations

[7] In meteorological work, the convention for reporting wind directions is to label them by their respective *upwind* directions. For example, “northerly” winds blow from north to south. In geological work, it makes more sense to label features either by the direction of transport or by the dip direction. Applying geological methods to aeolian work leads to identifying the orientations of dunes and other features by their *downwind* directions. For example, “southerly oriented” slipfaces, yardangs, ventifact grooves, etc. are formed by “northerly” winds as defined above. In aeolian work, both conventions are used simultaneously [e.g., Greeley *et al.*, 2003; Greeley and Thompson, 2003].

[8] In this work, we compare modeled wind directions to measured feature orientations using both conventions. Where describing winds, we use the upwind terminology and refer to wind *directions*. Where describing aeolian features, we use the downwind terminology and refer to

feature *orientations*. Where possible, we have labeled both conventions on the axes in the figures.

2. MOC NA Observations of Proctor Crater Dunes

2.1. Measured Orientations

[9] This section summarizes results and conclusions drawn from Paper 1. Wind-aligned orientations are visible in at least three different types of aeolian features: in the large dark dune field in the center of the crater floor, in dust devil tracks that cover the floor during the spring and summer, and in small bright bedforms that are nearly ubiquitous on the crater floor. Each type of feature has formed on a different timescale, indicating either recent or ancient winds. For example, dust devil tracks form and are subsequently obliterated each year, and therefore the winds that move dust devils downwind must be currently active. However, the large dark dunes may move on timescales of thousands of years or more, and thus may reflect older winds. Some of the bright bedforms may be ancient stabilized features, possibly indicative of winds dating to hundreds of thousands of years or more. Each type of feature and the wind information it provides is discussed in detail below. A summary of the results is presented in Table 1.

2.1.1. Dark Dunes

[10] As discussed in Paper 1, the dark dune field in the floor of Proctor Crater (see Figure 1) displays three slipface orientations. Slipfaces are produced by two processes. Grains are lifted into saltation and/or suspension and carried

Table 1. Current Wind Regime in Proctor Crater Based on MOC NA Images

Wind	Locale	Features Reflecting Wind Direction	Time of Occurrence
Primary (WSW: $239^\circ \pm 18^\circ$)	entire crater floor	dune slipfaces, bright duneforms dust devil tracks	fall and winter afternoon geostrophic-induced westerlies (strong) spring and summer early afternoon westerlies from planetary rotation (weak)
Secondary (ESE: $110^\circ \pm 18^\circ$)	central and western portion of dune field	dune slipfaces	?
Tertiary (ENE: $75^\circ \pm 9^\circ$)	eastern portion of dune field, possibly eastern portion of crater floor	dune slipfaces, bright duneforms (?)	spring/summer evening katabatic flow (strong)

across the brink of a dune, falling out onto the lee side (grainfall). As the sand deposited by grainfall accumulates, it produces a bulge of sand near the dune brink that eventually oversteepens and avalanches (grainflow) [e.g., *McDonald and Anderson*, 1995; *Nickling et al.*, 2002]. It is grainflow that is thought to control a dune's migration. Continued avalanching produces the characteristic slipfaces that are used both to identify dunes and to determine the wind direction. Slipfaces are always oriented transverse to the wind (i.e., they dip downwind).

[11] Figure 2a shows a rose diagram (i.e., a histogram on a polar plot) of the measured slipface dip orientations, or downwind directions, from Paper 1. For simplicity of presentation, the dune orientations have been binned by 10° increments. Each of the three slipface orientations is labeled with the mean and standard deviation of an interpreted formative wind direction. The three directions are labeled primary, secondary, and tertiary on the basis of their spatial frequency within the dune field. The primary dune slipfaces are created by winds from the WSW. These slipfaces are visible throughout the dune field. Falling dunes (sand accumulations on the downwind side of topographic obstacles) on the eastern sides of hills and cliffs southwest (i.e., upwind) of the dune field are aligned with this wind. This wind has been interpreted in Paper 1 as the wind that carried the dark dune sand to its current location from the southwest. The secondary slipfaces are consistent with winds from the ESE. They are prevalent throughout all but the easternmost portion of the dune field, and dominate in the form of transverse dunes along the west-northwest edge of the dune field. A large dark streak of sand emanating from the northern tip of the dune field is aligned with the secondary wind (see Figure 1). The tertiary slipfaces indicate winds from the ENE. These slipfaces are only present on the easternmost edge of the dune field, where they dominate dune morphology. The tridirectional wind regime observed in the Proctor Crater dune field is also a convergent wind regime, implying that the dune field resides in a location on the crater floor with zero or low net transport. As discussed in Paper 1, the reversing transverse and star dunes found in the dune field are consistent with the observed convergent wind regime.

[12] In most cases, individual images of dunes alone do not provide information on the season or local time of the winds that influence them. However, they do provide the directions of the winds that last influenced them, which may indicate dune activity ranging from saltation up to

and during the data acquisition to indurated surfaces that reflect ancient and now defunct wind systems. Therefore, in order to interpret the Proctor Crater dune slipface orientations in terms of the current wind circulation patterns, it must first be established that the dunes are currently active. The Proctor Crater dunes are free of dust accumulations that mantle the local surface each year, and although the surrounding crater floor becomes covered with dust devil tracks each spring and summer, the dunes display few such tracks. This suggests that the dunes are active, clearing away dust fallout with sand saltation, and that any dust devils that pass over dark sand leave behind no tracks because there is no dust left to be cleared away. Furthermore, the dune thermal inertia indicates the dunes are made of coarse-grained sand, consistent with previous measurements and predictions (see Paper 1). This also supports the idea that the dunes are neither covered in a dust mantle nor indurated: thick dust deposits on the dunes would lower the thermal inertia to a value consistent with dust grains (besides being unlikely based on the low albedo of the dunes), and dune cementation would increase the thermal inertia to a value too large to be indicative of sand-sized grains. In addition, there are few indications of hillslope erosion on the dunes (e.g., landslides suggestive of induration) or softening of slipface brinks, both of which are consistent with them being currently active. Thus the evidence suggests that each of the three measured slipface orientations corresponds to present-day winds.

2.1.2. Dust Devil Tracks

[13] Dust devil tracks were identified in most of the spring and summer images on the Proctor Crater floor. They form first over dark patches of sand in the springtime, eventually spreading over much of the crater floor as the season progresses. Tracks overlap one another but generally are not erased within a single summer season. By the following year the tracks have been erased, indicating that fresh tracks form each year after new dust fallout has accumulated on the crater floor.

[14] Most dust devil tracks are oriented WSW-ENE, with a great deal of variation (see Figure 2b). The vast majority of dust devil tracks were found during the spring and summer (see Figure 3). Dust devils are expected to form in the late morning to early afternoon during spring and summer when surface heating is maximum [e.g., *Ferri et al.*, 2003; *Cantor et al.*, 2002]. Because of a lack of obvious starting and ending points of the dust devil tracks, it is difficult to determine which direction the dust devils moved

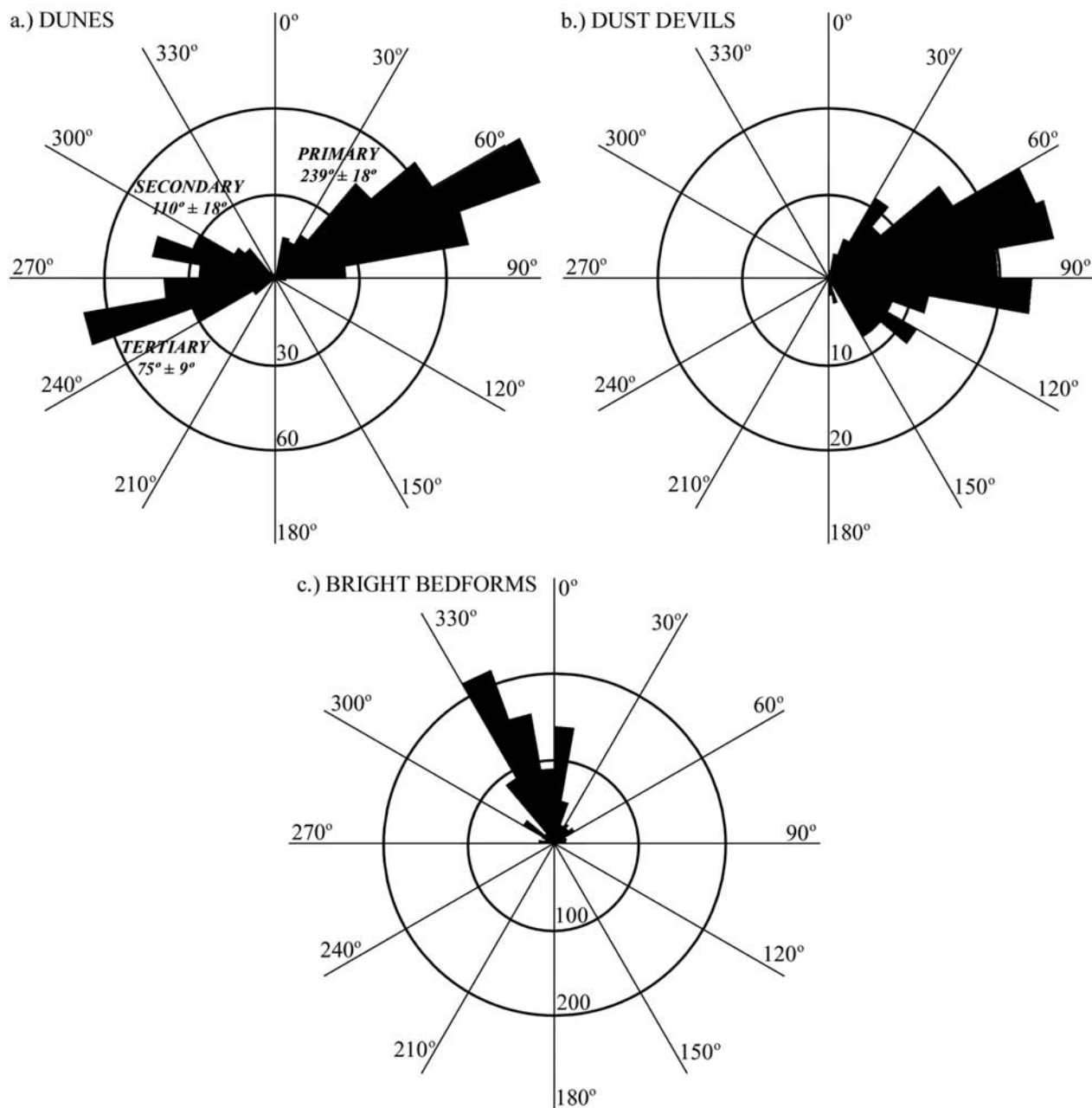


Figure 2. Rose diagrams showing the downwind azimuthal orientations of (a) dune slipfaces, (b) dust devil tracks, and (c) bright bedforms as measured in MOC NA images. The dune slipfaces are labeled with the mean and standard deviation of an interpreted upwind wind direction, and they are labeled “primary,” “secondary,” or “tertiary” on the basis of their spatial frequency throughout the dunefield. All measurements grouped into 10° bins. Note that in both Figure 2b and Figure 2c there is a directional ambiguity of 180° for each measurement owing to the difficulty of discerning upwind versus downwind direction.

and thus the ambient wind direction in the early afternoon during spring and summer. No dust devils with trailing tracks were imaged in Proctor Crater. However, as discussed in Paper 1, there is one springtime image showing dust devil tracks forming on a dark sand patch and moving downwind, pushed by winds from the WSW. Thus it is likely that all of the dust devil tracks, which most likely form in the same season and during the same time of day, indicate winds from the WSW.

[15] Dust devil tracks are visible throughout the (southern) spring and summer seasons in seventeen different MOC NA images. It is possible that the mean wind direction drifts as the season progresses, perhaps reflecting changes in the strength of Hadley circulation or tidal flow. Thus we measured the mean orientations of the dust devil tracks as a function of L_s , including tracks from newly released images acquired during the second Martian summer. Where the dust devil tracks were plentiful, only

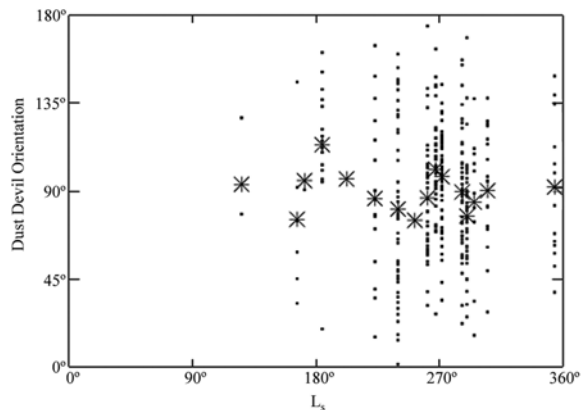


Figure 3. Dust devil track downwind orientation as a function of season. Dots represent individual track orientations; large stars indicate mean orientations across a single MOC NA image. Note that there is a directional ambiguity of 180° for each measurement owing to the difficulty of discerning upwind versus downwind direction. Most measurements fall within 45° – 135° , indicating tracks oriented between SW-NE and NW-SE.

the longest and most prominent tracks were measured. Where the dust devils were faint and scarce, as was the case for all wintertime tracks, all visible tracks were measured. No tracks were found in any autumn images. It is not clear whether tracks observed during the winter are fresh features or relict features from the previous summer season. As a result, there is a measurement bias toward larger, longer-lasting dust devils during the spring and summer and toward small and potentially old tracks during the winter. The results are shown in Figure 3, with small dots marking the orientation of individual dust devil tracks and large asterisks indicating the mean track orientation in each image. As with Figure 2b, all tracks are assumed to be oriented between 0° and 180° , thus avoiding the directional ambiguity. Although there is a wide distribution in track orientations, they generally tend to cluster between 45° and 135° . The mean orientations in each image are always near 90° . Both of these observations are consistent with the WSW-ENE orientation shown in Figure 2b. Thus, according to the MOC NA images, there is no observable change in dust devil orientation in Proctor Crater during the year, indicating that the mean daytime wind direction during the spring and summer and possibly during the winter is fairly constant.

2.1.3. Bright Bedforms

[16] Bright bedforms cover much of the floor of Proctor Crater. They are visible in the interdunes in the large dark dune field (see Figures 4a and 4b), suggesting that these features were present before dark sand entered the crater. Although they are an order of magnitude smaller (or more)

than the dark dunes, they are relatively immobile (see discussion in Paper 1), indicating that they are either smaller stabilized dunes or very large granule ripples [e.g., Sharp, 1963; Wilson and Zimbelman, 2004]. The TES bolometric albedos of these features range from 0.12–0.14, making them “bright” relative to the dark dunes that have an albedo ranging from 0.06–0.12. For these reasons, they are referred to in this work as “bright bedforms.” They are most likely some sort of ripple. There is an example shown in Paper 1 of a large dark barchan eroding bright bedforms as it slowly migrates by, only to have a few small features similar to the bright bedforms reform in its wake after it passed by. If these bedforms are in fact small dunes, then they would quickly migrate by the large dark dunes in an active wind regime, as dune migration rate is inversely proportional to the dune height (i.e., smaller dunes have less mass for the wind to move than larger dunes, and so they migrate faster). If most of the bright bedforms are simply stabilized relict dunes, then these features could not be recreated after being destroyed, as observed. Therefore these features are most likely very large granule ripples rather than sand dunes, and they may migrate more slowly than dunes and yet still remain active.

[17] The bright bedforms seem to be symmetric with no obvious slipfaces at the resolution of MOC NA images, making it difficult to determine whether they are aligned parallel or transverse to the local winds. Granule ripples are transverse to the wind [Sharp, 1963], so if these features are ripples, as proposed, then they are probably transverse as well. Figure 2c shows a rose diagram of the along-crest direction of the bright bedforms. If they are transverse then they were formed by winds from either the WSW or the ENE. These directions are consistent with both the primary and tertiary slipfaces found in the dark dunes. It is possible that where the primary winds dominate, the bright bedforms were created by winds from the WSW, and that where the tertiary winds dominate, the bright bedforms were created by winds from the ENE. Because in places the bright bedforms appear to lie stratigraphically below the dark dunes (see Paper 1), some of the bright bedforms may be ancient features, far older than the dark dune field. If this is the case then they may reflect ancient winds, indicating that wind circulation patterns have changed little since they were created.

2.2. Annual Slipface Reversal

[18] Although dune slipface orientations show the predominant wind directions that influence the dune field, they do not indicate the season or time of day in which these winds blow. In addition, the slipfaces do not indicate the age of the dune field. In fact, without evidence for recent dune movement, it is difficult to prove conclusively that these slipfaces were not formed by ancient winds that no longer blow, and that the dunes are not largely dormant. The paucity of erosional features on the dunes supports the idea

Figure 4. Reversing slipfaces on dunes at the eastern edge of the dune field. (a) MOC NA M19/00307 during the fall and (b) MOC NA E09/02707 during the spring show the same area with bright accumulations on opposing slipfaces. Figures 4c and 4d illustrate the locations of slipface brinks and bright accumulations. Figure 4e shows both sets of slipfaces and bright material. The movement of bright material is thought to be caused by a seasonal shift in wind direction. Note the slight shifting of one slipface brink in the upper right.

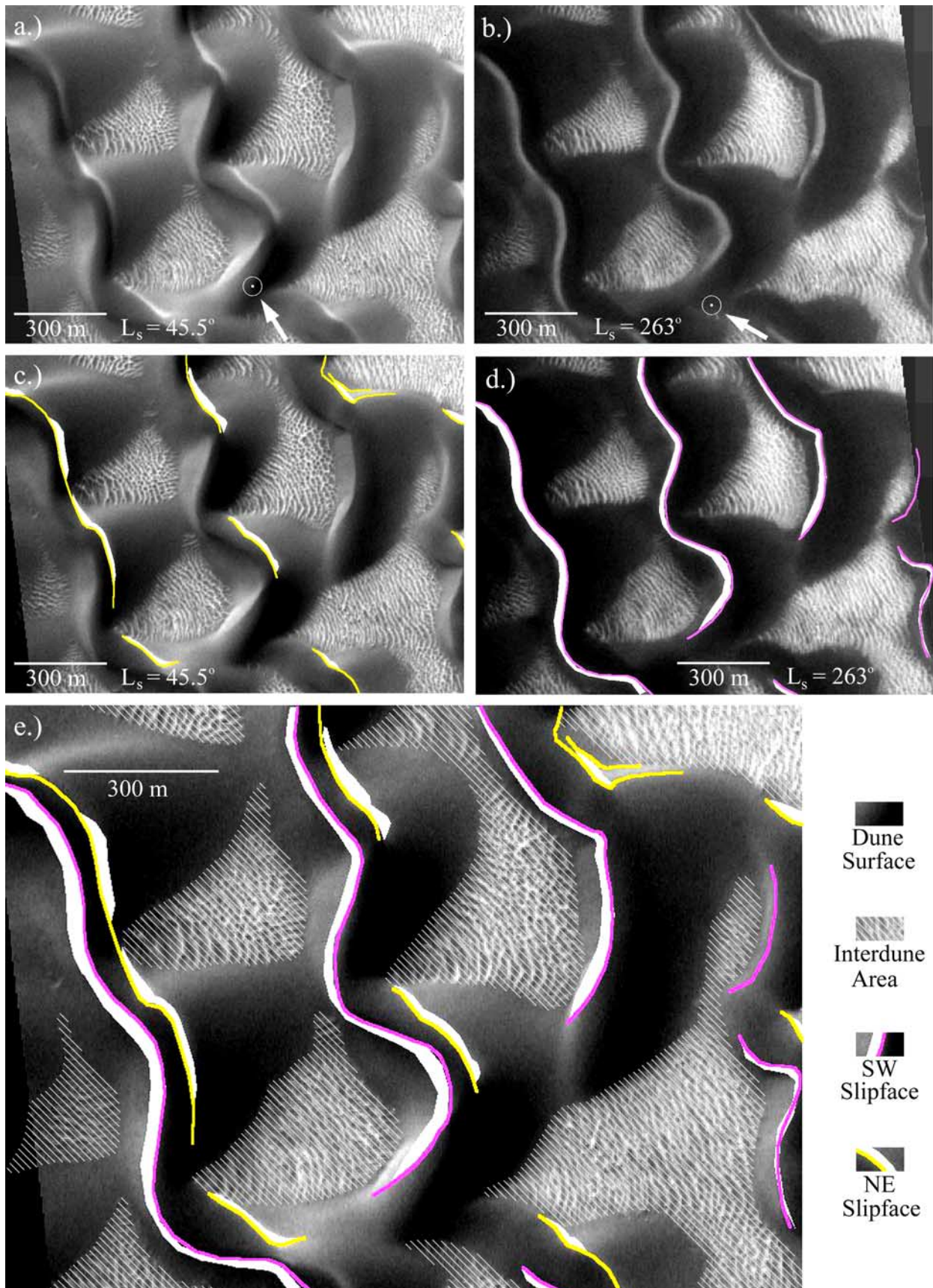


Figure 4

that the dunes are not stabilized, relict features (see, for example, Figures 41c and 41d of *Malin and Edgett* [2001]; are they slipface adjustments or erosional scars?). In addition, movement of dunes the size of those in the Proctor dune field could take a century or more to identify using data with the currently available image resolution, and thus their lack of observed movement in MOC and Viking images [e.g., *Malin and Edgett*, 2001] cannot be used to conclude that they are stabilized.

[19] However, there is evidence for slipface reversal in dunes on the eastern edge of the Proctor dune field that clearly indicates dune activity within the time span of the MGS mission (see Figure 2d and discussion from Paper 1). The eastern portion of the dune field consists of relatively smaller dunes with visible interdune areas, in contrast to the huge dunes atop a 50 m thick mound of sand found in the central and western-central portions of the dune field [see *Fenton*, 2003, Figure 12]. Because the eastern dunes are smaller than those in the center of the dune field, they have a smaller reconstitution time, thus the eastern part of the dune field may be a younger offshoot of the main accumulation of sand. At some point, winds from the southwest (the primary winds) blew sand from the main dune field to the northeast, where it was deposited upon encountering east-northeasterly winds (the tertiary winds), which only influence the eastern part of the dune field. Here the accumulation of dark sand is largely balanced between the primary and tertiary winds, producing reversing transverse dunes common to the dune field.

[20] In Paper 1, bright material was described on slipfaces of double-sided barchans at the eastern edge of the dune field. This bright material was attributed to the erosion of nearby underlying bright bedforms, which have a rounded appearance consistent with deflation and abrasion. It is only off the eastern edge of the dune field that the bright bedforms have this rounded appearance, and it is only at the eastern edge of the dune field that the dark barchans display bright slipfaces. This bright material cannot be residual frost because it is visible even in summertime images, when the surface is far too warm to support either CO₂ or H₂O frost.

[21] The slipface containing bright material switches sides of the double-sided barchans, as shown in Figure 4. Figure 4 compares two MOC Narrow Angle images of the same area at different times of the year. Figure 4a shows mid-fall frosted dune surfaces with bright material on northeast slopes. Figure 4b shows an overlapping image from the following year during the late spring, with fully defrosted dune surfaces bearing bright material on western slopes. Note that although the solar azimuth is similar in Figures 4a and 4b, the solar incidence angle is much lower (i.e., the sun is higher in the sky) in Figure 4b leading to fewer shadows and an increased emphasis on albedo contrast. The albedo contrast in Figure 4b is enhanced by the lack of frost cover present in Figure 4a. Figures 4c and 4d illustrate the slipface brinks and accumulations of bright material with colors corresponding to the formative wind directions (yellow is primary, magenta is tertiary). Figure 4e shows both slipface directions, emphasizing that they truly are on opposite sides of the barchans. The slipfaces on typical terrestrial reversing dunes switch sides with opposing (usually seasonally shifting) winds, erasing the old

slipface from the preceding season [e.g., *Sharp*, 1966; *Lindsay*, 1973]. In contrast to observations of terrestrial dunes, the dunes in Proctor Crater display both slipfaces at all times, indicating that neither slipface is fully erased by opposing winds. The survival of opposing slipfaces may be caused by some amount of internal cementation of the dune (providing resistance to wind erosion), or by the fact that the slipfaces are too large to be reworked in a single Martian year.

[22] In Figure 4c, one dune in the upper right corner of the image has two slipface brinks drawn on it. The more southwesterly and larger slipface corresponds to that in Figure 4a, and the smaller and more northeasterly brink corresponds to that in Figure 4b. This shift in slipface position probably indicates movement of this slipface toward the northeast between mid-fall and the following spring, although the dune itself has not shifted position. This movement indicates a shift of 13 to 37 m, depending on where along the brinks the movement is measured. Such a shift indicates strong and persistent seasonal winds. From one image to the next, no other slipfaces moved and no dunes changed position, suggesting that movement of this type is rare on a timescale of less than one Martian year.

[23] Figure 4 indicates that between mid-fall and late spring, the prevailing winds change direction and that both winds influence the dunes. Bright material is likely blown from the stoss (upwind) slope onto the slipface along with any loose dark sand from the dune surface. If the dark sand on the dunes is mobile then an explanation must be found for why mobile bright material does not mix with the dark sand as it moves back and forth over the dune. Rather, the bright material remains on the surface, unmixed and unburied. It is possible that the dark sand in the dune is somewhat indurated, and that only the bright sand is moving back and forth as the seasons progress. However, the thermal inertia of the Proctor Crater dunes is consistent with loose, coarse sand, not with indurated material, implying that the wind may be able to move the dark sand (see Paper 1 and references within). Because of its thermal inertia, some amount of dark sand most likely moves back and forth over the dune (along with bright material) as the winds shift. The bright material is likely sand that is more easily mobilized by the wind than the dark sand, and thus it is the last to settle onto the slipfaces as the winds decrease. This may indicate that the bright saltating material is made of smaller or less dense particles, causing them to saltate under lighter winds than the coarse basaltic grains comprising the dark sand.

[24] An alternative explanation is that the bright material is dust that settles in the wind shadow created by the dune (i.e., the slipface). In this case, suspended dust carried by the wind settles on the downwind side of obstacles: boulders, craters, and in this case, dunes. Like the bright sand hypothesis, the bright dust indicates accumulations on the downwind side of the dunes. However, an explanation must then be found for why the bright dust only accumulates on the eastern edge of the dune field throughout the Martian year. For this reason, we find the bright sand hypothesis to be more consistent with known theory.

[25] Six MOC Narrow Angle images pass over the eastern edge of the Proctor Crater dune field, imaging slipfaces at different seasons. Following the hypothesis that

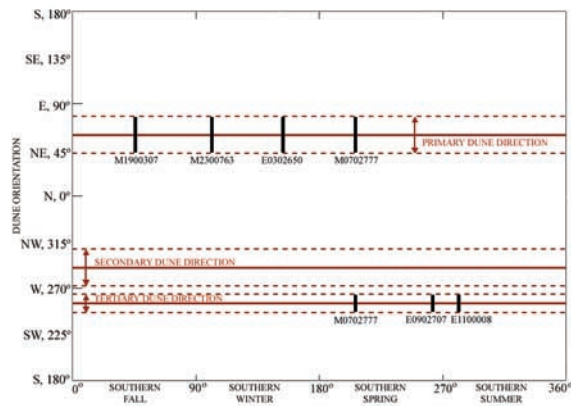


Figure 5. The L_s acquisition time of MOC NA frames showing accumulations of bright material on oppositely oriented slipfaces. Downwind dune orientations are indicated on the vertical axis. Horizontal red lines correspond to the three mean dune slipface orientations (shown in Figure 2a) and respective standard deviations. In (southern) fall and winter, the primary slipfaces have accumulations of bright material; in spring and summer, the tertiary slipfaces have such accumulations.

the bright material accumulates on the downwind side of the dunes, the dunes in this region are influenced currently by the primary and tertiary winds. Figure 5 shows each inferred wind direction as a function of L_s , labeled by the MOC NA frame in which it was found. The red lines mark the three mean and standard deviation dune slipface directions. Reading from this plot, the primary slipfaces are active throughout fall and winter, and the tertiary slipfaces are active during spring and summer. MOC frame M07/02777 from $L_s = 206.68^\circ$ appears to have bright material on both slipfaces, and likely indicates a transition time between the two seasonal wind regimes. As discussed next, the modeled winds reflect the activity of these slipfaces.

3. Mesoscale Modeling of Surface Winds

3.1. Mars MM5

[26] Mesoscale atmospheric models are tools that have recently been made applicable to Martian conditions. These models function similarly to Mars GCMs, but they can examine atmospheric patterns that vary from the synoptic (1000s km) down to the microscale (10s m). The goal of applying a mesoscale model to Proctor Crater is to determine how well predicted wind directions correlate with dune slipface orientations.

[27] We applied the Mars MM5, developed from the PSU/NCAR 5th Generation Mesoscale Model (MM5) by Toigo [2001]. The model is nonhydrostatic and uses terrain-following sigma coordinates. Initial and boundary conditions are provided by the Geophysical Fluid Dynamics Laboratory (GFDL) Mars general circulation model (GCM) [Wilson and Hamilton, 1996], which inherently couples the Mars MM5 to the GCM. The boundary layer parameterization scheme used in the Mars MM5 is that used in the Medium Range Forecast (MRF) [Hong and

Pan, 1996], which has been modified for Martian surface conditions [Toigo, 2001].

[28] Most of the Martian-specific parameterizations used in the Mars MM5 are taken directly from the GFDL Mars GCM. Radiative transfer is modeled using the scheme of Wilson and Hamilton [1996], which involves solar absorption by CO_2 and atmospheric dust of two particle sizes. The surface is represented by a MOLA topographic map [Smith et al., 2001]; albedo maps by Pleskot and Miner [1981], Paige et al. [1994], and Paige and Keegan [1994]; and thermal inertia maps from Palluconi and Kieffer [1981] and Vasavada et al. [2000]. Ground temperatures are calculated using a 12-layer subsurface heat diffusion model based on that used by the GCM [Wilson and Hamilton, 1996] and that uses initial temperatures from the GCM. Uncertainties in the model are difficult to quantify. Comparisons with Pathfinder and Viking lander temperatures match up well to the order of 5% or less, although wind velocities may be in error by as much as 25–50% [Toigo and Richardson, 2002].

[29] We ran twelve 10-day simulations equally distributed around the Martian year. Twenty-four pressure levels were defined, from near the surface (~ 50 m height) to the top at ~ 80 km above the surface. Shear stress, the force applied to the planetary surface by the atmosphere, is calculated on the basis of the winds at the lowest pressure level of the model and extrapolated to the surface. Horizontally, we used a 50×50 horizontal point grid with a resolution of 10 km. The grid was centered on Proctor Crater and it extended more than one crater diameter in each direction to avoid potential edge effects. The time step used in the simulations was 5 seconds, and parameters such as wind velocity and stress were saved once every hour as instantaneous values. In the past, hourly averaged values have been commonly used to provide a representative set of parameters. However, in this case the instantaneous values at the top of each hour were used instead to avoid washing out varying parameters that can be caused by using mean values.

[30] In order to achieve a horizontal grid spacing of 10 km, we nested the 50×50 point Proctor Crater domain in the GCM domain. This led to a resolution jump of a factor of 30, which is generally considered a fairly large difference. To test the reliability of this method, we later nested down to the Proctor Crater domain in three steps, never allowing a resolution jump of a factor larger than 5. In comparing the output from both model runs, we found that the end results are very similar and do not change the conclusions drawn in this paper, suggesting that using larger jumps in resolution while nesting domains may be more reliable than previously thought. We present results from the original model run only, unless otherwise specified.

3.2. Model Results

3.2.1. Seasonal Winds

[31] Because the strongest daily winds (winds with the highest stresses) are those that will move the most sand, it is these winds that will most affect dune morphology (see section 4.1 for a full discussion of the magnitude of modeled wind stresses). Therefore we first discuss the directions of the winds with the strongest daily stresses. These maximum winds are shown in Figure 6 as a function of L_s and wind direction. Daily maximum winds are indicated by black boxes with sizes that correspond to wind

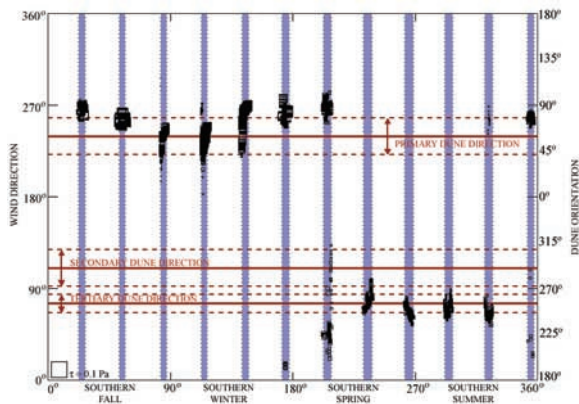


Figure 6. Maximum daily stresses from 25 model grid points located on the dune field. The symbol size indicates magnitude of stress. On the vertical axes, upwind wind directions are labeled on the left side, and downwind slipface orientations are labeled on the right side. Horizontal red lines correspond to the three mean dune slipface orientations (shown in Figure 2a) and respective standard deviations. Note the alignment of fall/winter wind with primary dune slipfaces and spring/summer winds with tertiary dune slipfaces.

stress, which is discussed in more detail in section 4.1. The time of year included in each model run is shown as a blue shaded strip. The three mean wind directions observed in the dune field and their standard deviations are indicated and labeled in red.

[32] The strongest daily winds shift in direction with the seasons. Fall and winter winds come from the west and west-southwest. Spring and summer winds blow from the east-northeast, but they are weaker than their fall and winter counterparts. The fall and winter winds correspond well with the primary dune slipfaces, and they are most likely responsible for both the dune slipfaces and the orientations of most of the bright bedforms that are common on the Proctor Crater floor. Dust devil tracks are also aligned with the primary wind, but they are generally only visible in spring and summertime images, indicating that the fall and winter wind is not responsible for creating the majority of dust devil tracks.

[33] The timing of the strongest winds compares well with the slipface reversal (compare Figures 5 and 6). Even the MOC NA frame M0/702777 that shows bright material on both slipfaces coincides with the season at which the strongest daily winds switch direction, indicating that this image has caught the dunes during a transition from one wind regime to the other.

[34] The dunes do become covered in frost during the winter, which may inhibit sand activity, precluding the winter winds from producing slipfaces. However, MOC NA images show fully frosted dunes only for the time period between $L_s = 50^\circ$ – 145° , with partial frost lasting until $L_s = 165^\circ$. According to the model results in Figure 6, the primary winds blow from $L_s = 350^\circ$ to 200° . Therefore, even if the frost cover temporarily stabilizes the dunes, the winds before and after the period of frost cover may account for the observed dune activity.

[35] The spring and summer winds from the ENE are aligned with the tertiary slipfaces. The winds in general are stronger during the winter, which likely indicates why they produce the most common slipfaces in the dune field. Further examination of the physics of saltation may explain why the tertiary winds have more control over the dunes they affect than the primary winds (see section 4.1).

[36] The secondary winds, from the ESE, are absent in the model results (see Figure 6). It is not clear why the ESE winds do not appear as the strongest winds at some point of the year, but it may be that they are produced by slightly weaker winds at some point during the day that does not appear in Figure 6 (i.e., there may be winds aligned with the secondary slipfaces, but they are not necessarily the strongest daily winds). Therefore, before we can state that the model does not predict the secondary winds, we must discuss wind direction and strength as a function of time over the course of the day.

3.2.2. Daily Winds

[37] To understand changes in winds during the day, we saved hourly winds when running Mars MM5 over Proctor Crater. The strongest daily winds correspond to two of the three observed dune slipface orientations, but we cannot explain the missing secondary winds that produce another dune slipface orientation in the dune field. In addition, examining only the strongest daily winds does not explain the orientation of dust devil tracks during the spring and summer, which seem to be oriented 180° from the strongest winds during that season. Examining hourly winds for each sol shows much more detail than the maximum (once/sol) wind that was plotted in Figure 6.

[38] Figure 7 shows the direction of winds over the Proctor crater dune field for each hour in each model run. A total of 25 grid points in the lowest pressure level in the model (nearest the ground) were located over the dune field, and each point is plotted in Figure 7. As with Figure 6, the three mean and standard deviation slipface orientations are marked, and the black boxes that indicate modeled winds are scaled by wind stress. Each model run is shown separately and labeled, although all ten days included in each run are shown in a single plot.

[39] The time of day of the maximum daily winds can now be resolved. Spring and summer model runs clearly show ENE (tertiary) winds during the evening hours (see Figures 7b–7e). Fall and winter winds from the WSW that are aligned with primary dune slipfaces are the strongest of the year, and they blow during the afternoon (see Figures 7g–7i). Figures 7a and 7l show the winds transition from later winter into early spring. In this period, the winter winds from the WSW weaken while winds nearly out of the north dominate the evening hours. As spring progresses, these northerly winds shift to the ENE and become the tertiary winds that last throughout the spring and summer seasons. Figures 7f and 7g show the winds transition from late summer into early fall. Afternoon winds from the WSW become stronger, while the ENE evening winds rotate and become northerly winds that die out as fall progresses.

[40] Dust devils are expected to form in the spring and summer, during the late morning through the early afternoon. Model runs from these times predict winds that range through all 360° , but they generally cluster between NW and SW (see Figure 7a–7f). These winds correspond well to

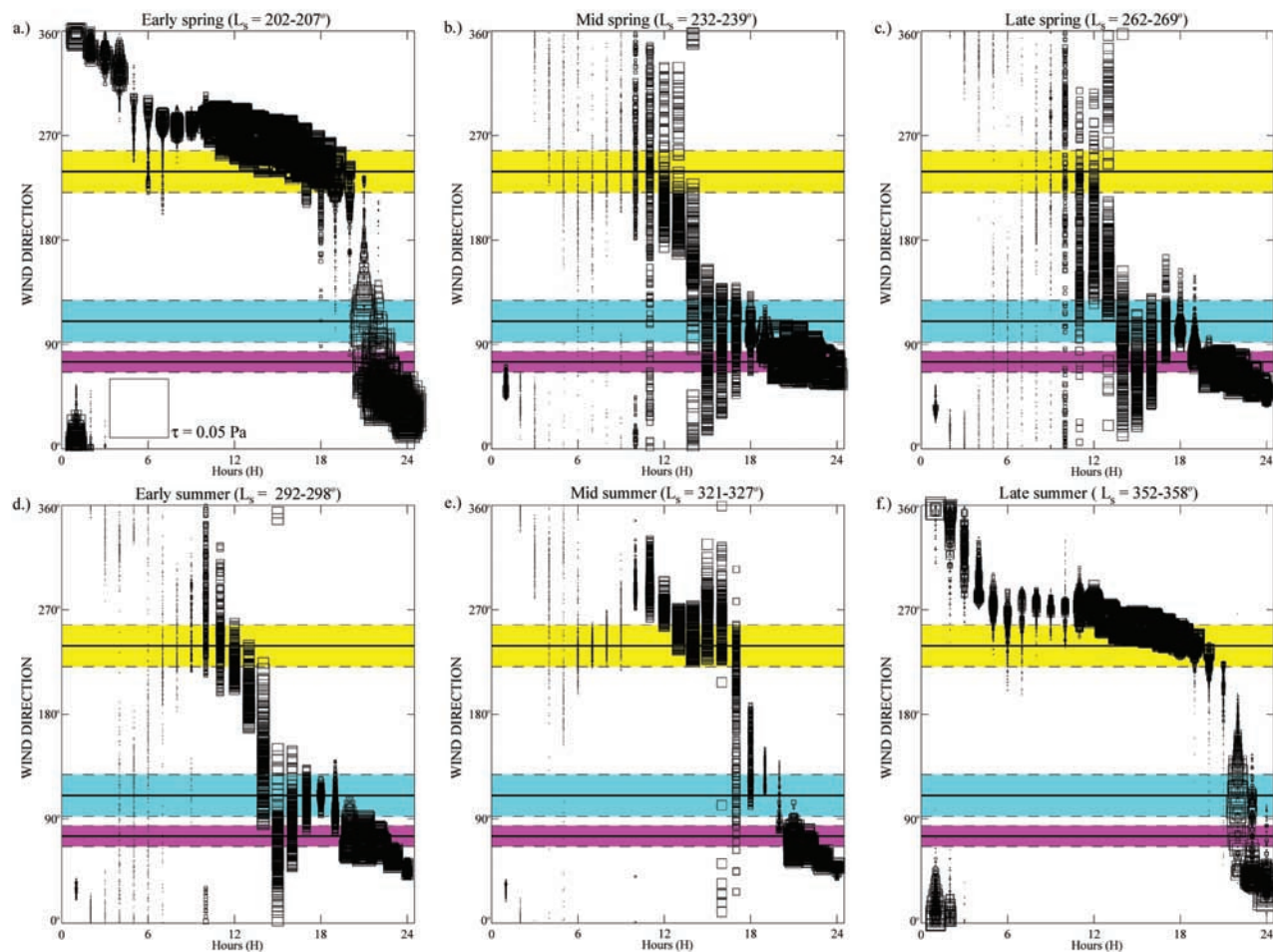


Figure 7. Modeled hourly wind directions over the dune field for each model run. Data symbols are scaled by the magnitude of stress. Primary, secondary, and tertiary slipface directions (mean and standard deviation) are plotted as yellow, magenta, and blue, respectively. The wind directions and strengths shift dramatically between spring/summer and fall/winter, with transition periods in between. Note the correspondence of daytime fall/winter winds to the primary dune slipfaces and evening spring/summer winds to tertiary dune slipfaces.

the 45° – 135° orientation range shown for dust devil tracks in Figure 3 (see also discussion in section 2.1.2). The winds also resolve the directional ambiguity of the dust devil tracks, supporting the previous conclusion that the dust devils were formed in a wind regime that blew generally from the west. Furthermore, there is no temporal drift in wind direction throughout the spring and summer seasons, although the spread in wind directions becomes tighter in the transitions both from winter and into fall (see Figures 7a and 7f). Generally, the uniform spread in spring and summer noontime winds is consistent with the lack of directional trend observed in dust devil tracks (see Figure 3).

[41] None of the daily winds indicate any alignment with slipfaces oriented to secondary winds, suggesting that perhaps these winds no longer blow. However, the slipfaces made by ESE winds are crisp and uneroded, implying that they are probably not relics of an old wind regime. There are winds that briefly align with these secondary winds during the time of transition between the winter and summer circulation patterns (see Figure 7 at $L_s =$

352° – 358° and 172° – 178°) and in the late afternoon during the summer (see Figure 7 at $L_s = 232^{\circ}$ – 239° , 262° – 269° , and 292° – 298°). But these winds are not strong and do not appear to be part of any persistent wind pattern. It may be that a full year's run would produce a time when the secondary winds dominate, although the model runs here appear to be fairly representative of modeled winds throughout the Martian year (i.e., winds from one model run to the next change relatively smoothly, so it does not appear that any large wind patterns have been skipped over). Possible explanations for the missing secondary wind are discussed in section 4.3.

4. Discussion

4.1. Wind Stresses

[42] Although the modeled winds may align with observed wind features, only winds above a particular threshold stress value are strong enough to initiate saltation. Some wind features, such as dust devil tracks, do not rely on ambient

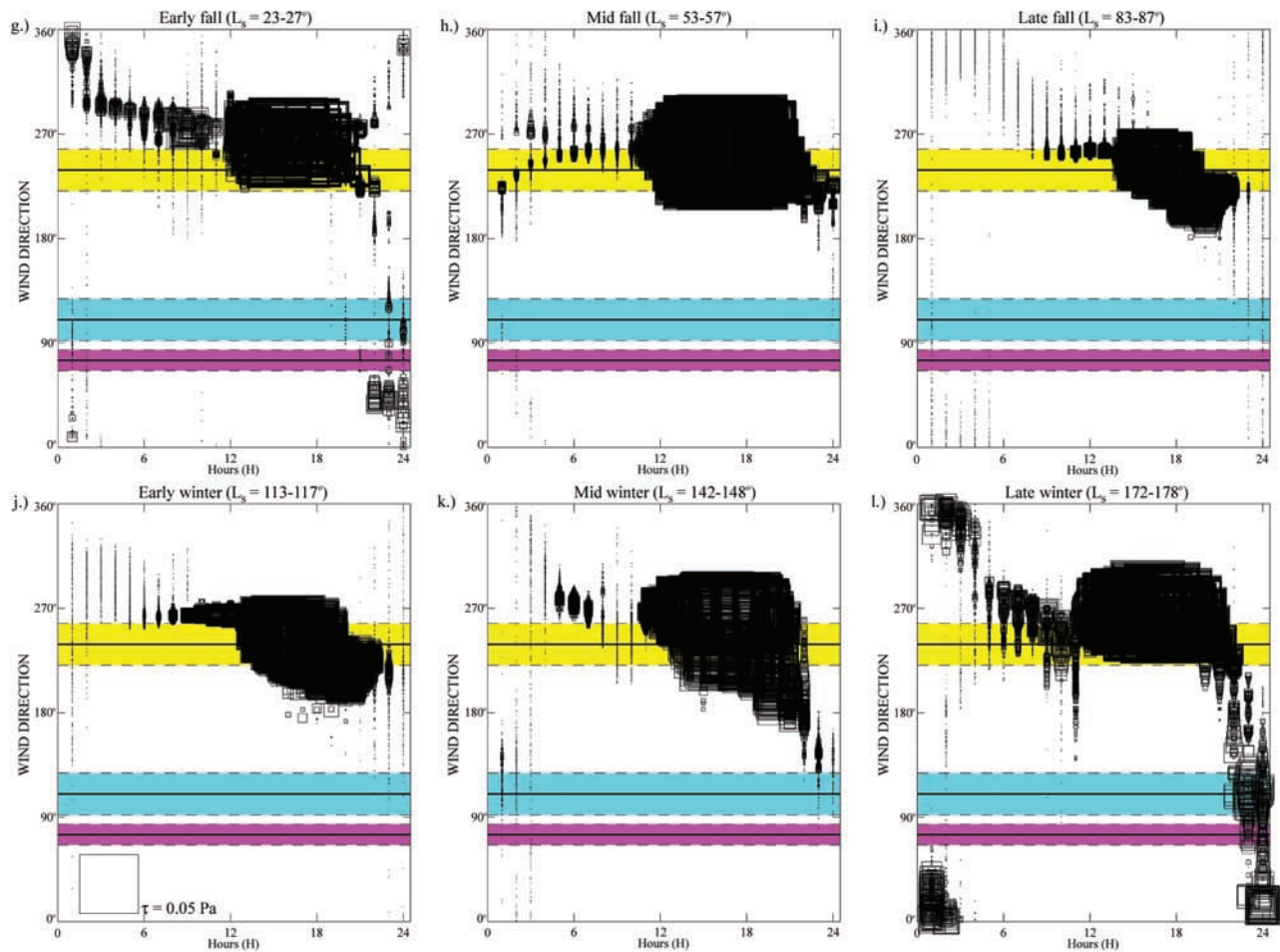


Figure 7. (continued)

wind stress alone, and in these cases the modeled stress is not a directly relevant parameter. However, saltation initiation is important for explaining features such as dunes, which are morphologically controlled solely by sand saltation. *Iversen and White* [1982] conducted wind tunnel experiments, finding an empirical relation for the saltation threshold under Martian atmospheric conditions. They found that the threshold varied as a function of particle size, particle density, atmospheric temperature, and atmospheric pressure. Because the saltation threshold is sensitive to so many parameters, it is crucial to constrain these values in order to determine whether the mesoscale model truly predicts the saltation of sand within the Proctor Crater dune field.

[43] In Paper 1, thermal inertia values derived from TES [Christensen *et al.*, 2001] led to an estimated effective sand grain size for the Proctor Crater dunes of $740 \pm 170 \mu\text{m}$. Although this grain size is very coarse for terrestrial dune sand, it is consistent with previous estimates of the Proctor Crater dune sand (see Paper 1 for discussion and references within). In addition, the compositional analysis described in Paper 1 indicated that the dune field is almost exclusively composed of basalt grains, where the basalt is inferred from the identification of pyroxene and plagioclase in TES spectra. In this work we assume the grains have a density

typical of terrestrial basalt (3200 kg m^{-3}), although it is possible that the sand could be composed of grains with a lower bulk density (e.g., scoria).

[44] In the relation by *Iversen and White* [1982], the threshold stress for saltation varies as a function of both air temperature and air pressure. For a constant pressure, a lower temperature has a lower threshold stress; for a constant temperature, a higher pressure has a lower threshold stress. Thus conditions for sand saltation are optimized under conditions of low temperature and high pressure. Figure 8 shows predicted atmospheric conditions for two of the twelve model runs. The upper, solid curve in Figures 8a–8d shows estimated fluid threshold friction velocities and fluid threshold stresses using model output temperatures (Figures 8e and 8f) and pressures (Figures 8g and 8h), and assuming that the sand grains moved by the wind are $740 \mu\text{m}$ diameter lithic fragments of basalt. The left-hand column corresponds to six days of model runs during the coldest time of year ($L_s = 90^\circ$) and the right-hand column corresponds to six days of model runs during the warmest time of year ($L_s = 270^\circ$). The lower, solid curve in Figures 8a–8d indicates the impact stress threshold, or the stress necessary to saltate grains from the impact of already saltating grains. The impact stress threshold may be considered roughly equivalent to ~ 0.8 that of the fluid stress

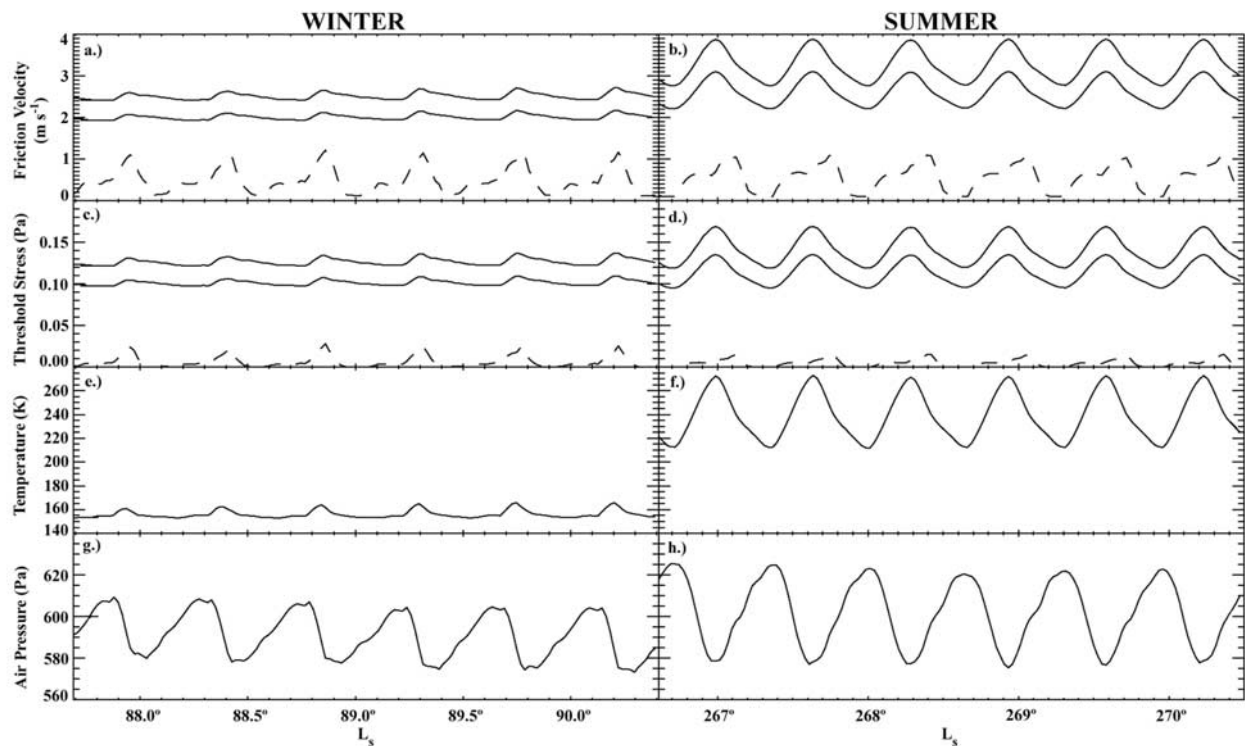


Figure 8. Atmospheric conditions over the course of six days for two of the twelve model runs. (a) Friction velocities under wintertime conditions predicted from model runs. Upper solid line: fluid friction velocity; lower solid line: impact friction velocity ($0.8 \times$ upper line); lower dashed line: actual predicted wind friction velocities. (b) Same as Figure 8a for summertime conditions. (c) Stresses under wintertime conditions predicted from model runs. Upper solid line: fluid threshold stress; lower solid line: impact threshold stress ($0.8 \times$ upper line); lower dashed line: actual predicted wind stresses. (d) Same as Figure 8c for summertime conditions. (e.) Wintertime air temperatures of lowest level in model runs. (f) Same as Figure 8e for summertime conditions. (g) Wintertime air pressure of lowest level in model runs. (h) Same as Figure 8g for summertime conditions. Threshold stresses and friction velocities calculated from *Iversen and White* [1982]. Note the diurnal variations in temperature and pressure, leading to shifts in threshold stress values, possibly indicating that daily variations in atmospheric conditions are more important than seasonal variations in determining the movement of sand by the wind. Note also that the model runs never predict winds strong enough to blow above the threshold values (dashed lines in Figures 8a–8d).

threshold [Bagnold, 1941; Anderson and Haff, 1988; Toigo *et al.*, 2002]. Because movement from such impacts is the mechanism that causes most grains to saltate, the impact stress threshold is considered to be the most representative threshold stress value. The dashed line in Figures 8a–8d shows the predicted friction velocities and wind stresses.

[45] There are several things to note in Figure 8. First, both the temperatures and pressures vary diurnally. During the winter, the air temperature oscillations range from ~ 150 K to ~ 165 K and are dampened by the presence of a seasonal CO_2 ice cap on the surface, which strongly controls the overlying air temperature (Figure 8e). During the summer, no ice cap is present, and the temperatures swing between ~ 210 K and ~ 270 K from night to day, respectively (Figure 8f). Wintertime pressures (Figure 8g) vary between ~ 570 and ~ 610 Pa, but they are somewhat moderated by the underlying seasonal ice cap. During the summer the air pressure is somewhat higher (Figure 8h),

varying between ~ 575 and ~ 625 Pa. The diurnal and seasonal variations in temperature and pressure lead to variations in the threshold stress for saltation. During the winter, low air temperatures and air pressures only slightly lower than summertime values lead to estimated threshold stress values slightly lower than those calculated for average summertime conditions. The highest daily pressures in the winter occur after peak daily temperatures (probably caused by partial sublimation of the underlying seasonal ice cap), but before the daily temperature lows. Because the temperatures and pressures are out of phase over the course of a day, the estimated threshold stresses only vary between 0.095 Pa and 0.105 Pa, a shift of $\sim 10\%$. In contrast, the summertime temperatures and pressures are 180° out of phase: in the nighttime hours, the lowest temperatures coincide with the highest air pressures. These conditions at night combine to lower the threshold stresses from their mid-day peak of 0.135 Pa to 0.095 Pa, a shift of nearly 30%. Thus seasonal variations in atmospheric conditions may not

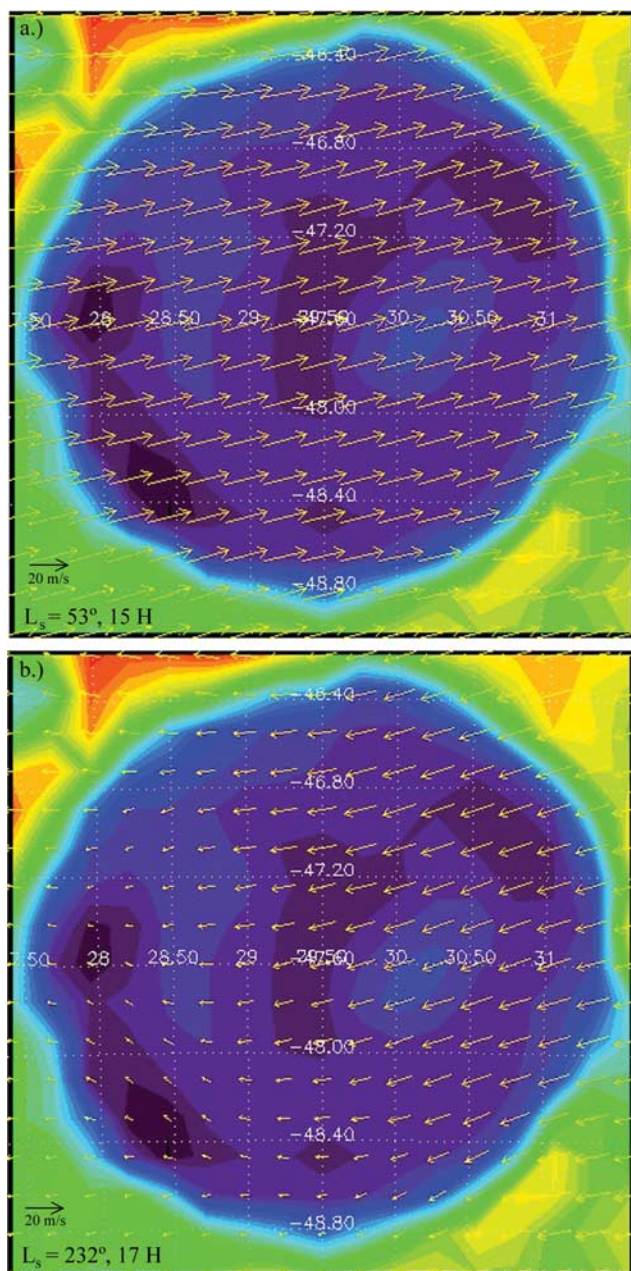


Figure 9. Surface wind vectors illustrating (a) primary winds during the afternoon in the fall and (b) tertiary winds in the evening during spring. The background is a color map of topography, with violet, blue, green, yellow, orange, and red indicating successively higher elevations. The dark dune field is indicated by a local topographic high at 30.2°E , 47.7°S .

be as important as daily variations in determining the capacity of the wind to saltate sand on Mars.

[46] The second point of note is that the predicted wind stresses in both of these model runs (and indeed in all twelve model runs) are less than any of the calculated threshold stresses (see dashed lines in Figures 8a–8d). Although winds predicted by the Mars MM5 are well aligned with two observed slipface orientations, the calculated wind stresses are not high enough to predict sand

saltation. There are a number of reasons why the model may not be predicting winds that are strong enough to saltate sand. The first and most obvious reason is that the grid spacing of 10 km by 10 km is too large to capture local wind gusts, with each grid point representing an average predicted wind over a 100 km^2 area. This is a problem that has plagued modelers applying GCM wind predictions to sand saltation on Mars [e.g., Greeley *et al.*, 1993; Anderson *et al.*, 1999; Toigo *et al.*, 2003]. A recent sensitivity study of model resolution in a terrestrial mesoscale model indicates that predicted wind stresses are more accurate at higher resolutions in which the topography is better defined [Liu and Westphal, 2001]. Thus model resolution appears to be a significant factor in predicting wind strength, and this may be the case for our model runs as well. To mitigate against this, wind gusts may be modeled with a Weibull distribution [e.g., Seguro and Lambert, 2000], which assumes a probability distribution of wind speeds with given wind conditions, the upper end of which may account for a large percentage of the actual sand flux. This correction factor, while dependent on empirical data that may or may not be applicable to Martian conditions, is beginning to be studied for use with Mars atmospheric models [Newman *et al.*, 2002]. A second possibility is that during the model runs, although the time step was 5 seconds, we only saved winds from the top of each hour to conserve disk space. It may be that winds above the saltation threshold would have been captured if instead the strongest winds of each hour were considered; rare wind gusts may produce saltation.

4.2. Spatial Variation and Origin of Winds Aligned With Aeolian Features

[47] The primary winds appear to influence dunes, falling dunes, and bright bedforms throughout the interior of Proctor Crater. The tertiary winds only affect the eastern edge of the dune field and perhaps the orientations of some of the bright bedforms in the eastern portion of the crater floor. Modeled winds should reflect this spatial pattern if they truly represent actual surface winds.

[48] Figure 9 shows two maps of instantaneous winds. The winds are superimposed on a MOLA elevation map, with violets and blues indicating low elevations. The dune field is visible as a lighter blue mound at 30.2°E , 47.7°S . Figure 9a shows afternoon winds during fall, when the primary winds are strongest (see Figure 7). The arrows represent the velocities of the lowest-level winds, at a height of $\sim 50\text{ m}$. The winds across the whole area blow from the WSW, indicating that the primary winds do in fact influence the entire crater floor. These fall and winter winds are midlatitude westerlies created by a geostrophic wind (created by balancing the Coriolis force with the pressure gradient force) that is strengthened by the strong latitudinal temperature gradient present in the winter hemisphere. The slight rotation to the south is caused by the presence of the Hellas basin some 900 km to the east, which creates intense slope winds that deflect the approaching westerly winds [Joshi *et al.*, 1997].

[49] Figure 9b shows another wind map, this time from the early evening hours during the spring. Strong winds (on the order of $\sim 20\text{ m s}^{-1}$) from the east-northeast dominate the eastern portion of the crater. These are the tertiary winds that control dune morphology on the eastern

edge of the dune field. As the evening progresses, the ENE winds sweep across the crater floor until they are the sole winds blowing in this area (not shown), but these winds are most sustained in the eastern part of the crater floor. This set of winds is caused by the diurnal tide, in which winds east of the subsolar (noonday) point surge toward this point to fill the volume of low pressure caused by rising air in the summer noontime heat. Furthermore, as the ENE winds cross the eastern rim of Proctor Crater, they encounter relatively warmer air rising from the crater floor ~ 1500 m below. The air spills beneath this lighter air into the crater in a katabatic flow, accelerating down and across the crater floor. It is these winds that explain why sand has become trapped in Proctor Crater: the primary winds blew sand into the dune field from the WSW, but the sand stopped when it encountered the tertiary winds from the ENE that effectively stop dune migration to the east. Sand outside the crater does experience ENE winds at this time of year, but on the intercrater plains these winds are not enhanced by topography as they are in the floor of Proctor Crater, and so not as much sand has accumulated on the intercrater plains.

[50] Another way to show the spatial distribution of wind directions across the dune field is to show rose diagrams for each grid point in the model run. Figure 10a shows a rose diagrams for individual grid points, summed over each of the twelve model runs, in the area overlying Proctor Crater. Figure 10c shows the same for the dune field only. The histograms show frequency of wind direction without regard to wind strength, and thus they emphasize wind persistence. Note that these plots show the winds' *downwind* directions, in order to more directly compare them with the orientations of the dunes (Figure 2). The outer black ring in Figure 10a outlines the Proctor Crater rim, and the smaller inner ring (and the ring in Figure 10c) defines the edge of the dune field. Note that the scale of the histograms, marked on the left, varies from one plot to the next (e.g., 1x, 2.4x, 4x, 8x). In most areas of the crater floor, winds from the WSW dominate over all other wind directions throughout the year. In no cases are secondary winds, from the ESE, present in any quantity. In the northwest and southeast edges of the crater floor, a northwesterly wind is present, but it is not reflected in any observed aeolian feature on the surface. These winds may be too weak to carry sand or scour material from the surface, but they do occur frequently enough to appear on this figure.

[51] A better way to emphasize the variation in wind direction is to subtract from all grid points the histogram from a single control grid point. Figure 10b shows the cumulative winds over Proctor Crater at each grid point minus the winds at the control point, which we chose from the center of the dune field (marked in boldface). Figure 10d shows the same for the dune field area only. Thus all of the differenced rose diagrams show winds with respect to those predicted over the center of the dune field. Compared to Figure 10a, the variation in wind direction from point to point in Figure 10b is much more visible. The center of the crater has winds fairly similar to those observed on the dune field. The northwesterly winds at the northwestern and southeastern edge of the crater are much easier to discern. Tertiary winds from the ENE are clearly more common in the eastern portion of the crater floor, and on the eastern

edge of the dune field, precisely where aeolian features in MOC images indicate that they exist. The primary winds are more persistent at the edge of the crater, in the southwest, than elsewhere, which may indicate that more erosion and sand migration is occurring near the edge of the crater floor than downwind near the dune field.

[52] On the northwest edge of the dunes, there are transverse dunes that are aligned with the mysterious secondary winds. This is the portion of the dune field in which the secondary-facing dune slipfaces dominate. The ESE winds in Figure 10d are caused by winds in transition from one dominant direction to another. For example, modeled winds correlate with the secondary winds in the late afternoon during spring and summer as winds shift from the early and mid afternoon WSW winds that produce dust devil tracks to the evening ENE tertiary winds (see Figures 7b–7d). In addition, modeled winds aligned with the secondary winds occur in the evening during the seasonal transition from the winter to summer wind regime (see Figures 7a and 7l) and again during the transition from the summer to the winter wind regime (see Figure 7f). The winds are not strong in either case, and they do not persist in the direction of the secondary winds for any length of time. Thus although some winds aligned with the secondary winds are predicted by the model, they are not likely responsible for forming the observed slipfaces.

4.3. Missing Secondary Winds

[53] The Mars MM5 model runs predict and provide a reasonable explanation for the wind patterns that created two of three observed dune slipface orientations as well as dust devil track orientations. However, it does not produce winds of any strength or duration matching a third dune slipface orientation. One possible explanation for the missing secondary winds is that the Mars MM5 model runs covered too small of a domain and thus did not account for regional effects that might influence wind directions, such as the deep Hellas basin 900 km to the east. One way to check for such an inconsistency is to compare the Mars MM5 results to those from a GCM. Although the GCM winds would not capture the local-scale fluctuations the mesoscale model is designed to predict, it would confirm the regional wind patterns that may drive the winds predicted by the Mars MM5. Alternatively, there may be unusual but strong storms that occasionally pass through the area, with wind gusts that carry large quantities of sand. Such storms may be infrequent enough that they are not predicted by GCMs, but of enough strength that the secondary slipfaces are maintained.

[54] The primary and tertiary winds, as well as the WSW summer winds that produce dust devil tracks, are visible in GCM wind predictions as well as in Mars MM5 model runs. *Fenton and Richardson* [2001] made global predictions of surface winds using the GFDL Mars GCM. In that work they found that the average southern fall and winter winds at the location of Proctor Crater (47.5°S, 30°E) range from the WNW to WSW, fairly consistent with the primary winds [see *Fenton and Richardson*, 2001, Figures 1a and 1b]. Summer evening winds come from the ENE following the diurnal tide, and summer afternoon winds come from the WSW following a deflection of Hadley circulation winds

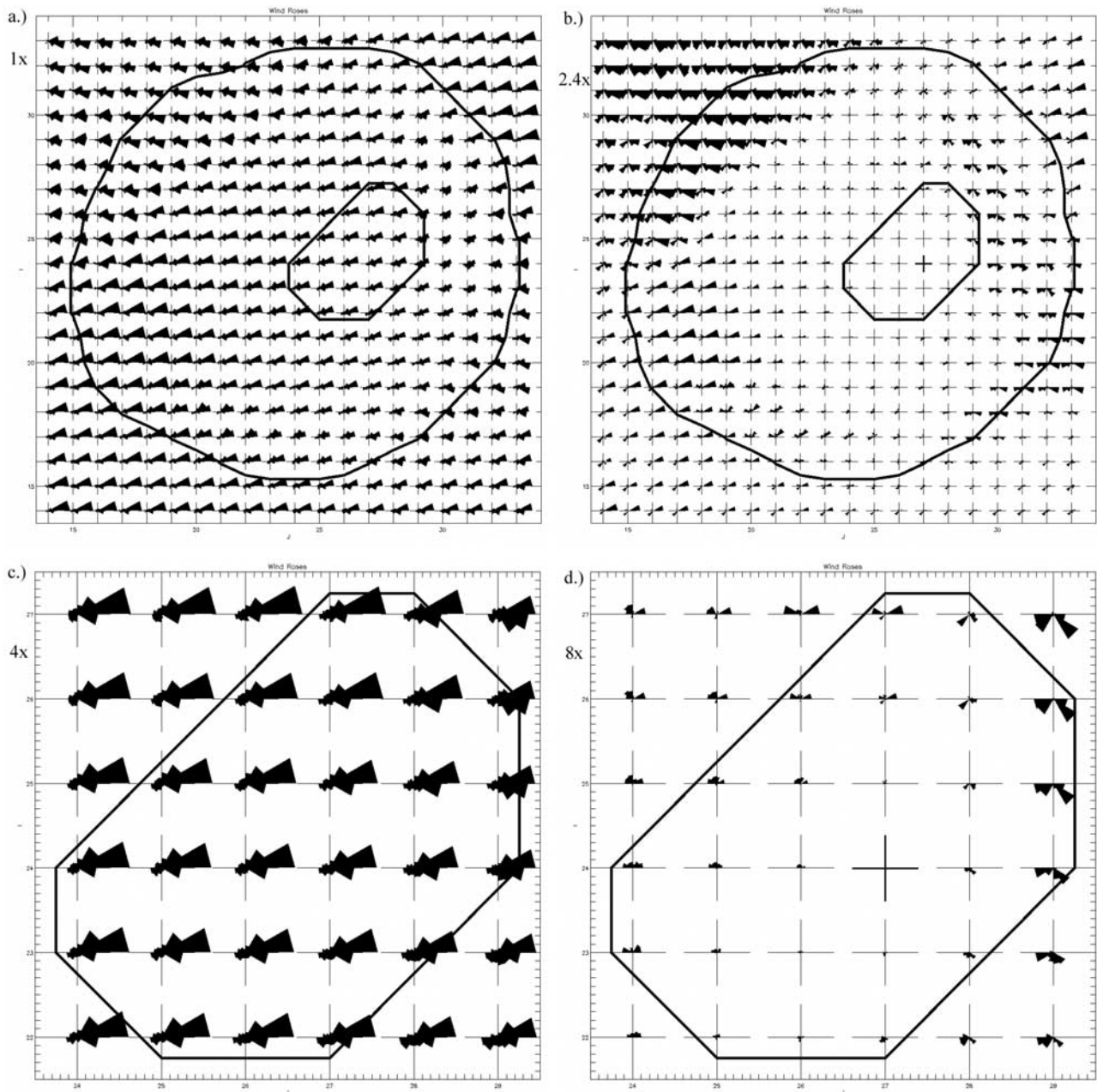


Figure 10. (a) Rose diagram of all wind directions in all model runs for each grid point across the crater and (b) the same differenced with a control rose diagram from the center of the dune field (marked in boldface). The crater rim and dune field are outlined in black. Figures 10c and 10d show the same as Figures 10a and 10b, zoomed in on the dune field. The scale of the histograms, marked on the left, varies from one plot to the next (e.g., 1x, 2.4x, 4x, 8x). Note that these diagrams indicate *downwind* direction for easy comparison with aeolian feature measurements in Figure 2.

[see *Fenton and Richardson, 2001, Plates 1c and 1d*]. The daytime wind that *Fenton and Richardson [2001]* found matched the orientations of bright streaks, and it is considered responsible for creating dust devil tracks. The evening wind that they found matched the orientations of dark streaks is the tertiary wind that is considered to produce one of the dune slipface orientations. Modeled winds aligned with the secondary winds are absent from the GFDL Mars GCM runs as well as the Mars MM5 runs described here. Therefore the Mars MM5 runs are consistent with

global model results, and no large-scale effects have been erased by the use of a small domain.

5. Conclusions and Future Work

[55] Apart from the missing secondary wind (from ESE), the Mars MM5 successfully predicts all other wind directions indicated by aeolian features on the surface. We attribute the winds (from WSW) that align with the primary slipfaces to fall and winter afternoon westerlies that dom-

inate the crater floor. We also attribute the winds (from ENE) that align with tertiary slipfaces to spring and summer evening easterly katabatic flows that are concentrated in the eastern portion of the crater floor. These tertiary winds may also explain the trapping of sand in crater floors, for they oppose the primary winds that move sand through the area. The tertiary winds are present throughout the region but they may only be strong enough on the crater floors to counter the strong primary winds, thus producing a convergent wind regime that forces sand to accumulate. Dust devil tracks are proposed to be produced by weak early afternoon westerly spring and summer winds. The Mars MM5 results provide a possible explanation for the source of the winds that produce aeolian features, making it a useful tool for understanding and predicting aeolian processes on the Martian surface.

[56] Future work may help to resolve the remaining discrepancies between the dune morphology and modeled winds. If the missing winds (from the ESE) that produce the secondary dune slipfaces form by a common annually reproduced wind pattern (as opposed to an infrequent storm that the atmospheric models cannot predict), then a method must be found for discovering why they are not represented in this work. A number of other craters in Noachis Terra also contain dune fields, each of which has slipfaces indicating the strongest surface winds that influence the area. If these secondary winds persist throughout the region, perhaps to different degrees in different dune fields, then an understanding of the regional distribution of winds can be gained. A potential way to resolve the issue of the missing wind is to model winds over nearby craters to determine if these secondary winds are predicted elsewhere, and how well those predictions match the dune morphology.

[57] **Acknowledgments.** We would like to thank Arden Albee for a helpful review of the manuscript and Shawn Ewald for keeping the model chugging along. We also thank Nicholas Lancaster and an anonymous reviewer for a thorough review and much constructive criticism. This work was funded by NASA grant NAG5-11257, part of the Mars Data Analysis Program.

References

- Anderson, F. S., R. Greeley, P. Xu, E. Lo, D. G. Blumberg, R. M. Haberle, and J. R. Murphy (1999), Assessing the Martian surface distribution of aeolian sand using a Mars general circulation model, *J. Geophys. Res.*, *104*(E8), 18,991–19,002.
- Anderson, R. S., and P. K. Haff (1988), Simulation of eolian saltation, *Science*, *241*, 820–823.
- Arvidson, R. E. (1974), Wind-blown streaks, splotches, and associated craters on Mars: Statistical analysis of Mariner 9 photographs, *Icarus*, *21*, 12–27.
- Bagnold, R. A. (1941), *The Physics of Blown Sand and Desert Dunes*, Methuen, New York.
- Cantor, B., M. Malin, and K. S. Edgett (2002), Multiyear Mars Orbiter Camera (MOC) observations of repeated Martian weather phenomena during the northern summer season, *J. Geophys. Res.*, *107*(E3), 5014, doi:10.1029/2001JE001588.
- Christensen, P. R., et al. (2001), Mars Global Surveyor Thermal Emission Spectrometer experiment: Investigation description and surface science results, *J. Geophys. Res.*, *106*(E10), 23,823–23,871.
- Cutts, J. A., and R. S. U. Smith (1973), Eolian deposits and dunes on Mars, *J. Geophys. Res.*, *78*(20), 4139–4154.
- Fenton, L. K. (2003), Aeolian processes on Mars: Atmospheric modeling and GIS analysis, Ph.D. thesis, 215 pp., Calif. Inst. of Technol., Pasadena.
- Fenton, L. K., and M. I. Richardson (2001), Martian surface winds: Insensitivity to orbital changes and implications for aeolian processes, *J. Geophys. Res.*, *106*(E12), 32,885–32,902.
- Fenton, L. K., J. L. Bandfield, and A. W. Ward (2003), Aeolian processes in Proctor Crater on Mars: Sedimentary history as analyzed from multiple data sets, *J. Geophys. Res.*, *108*(E12), 5129, doi:10.1029/2002JE002015.
- Ferri, F., P. H. Smith, M. Lemmon, and N. O. Renno (2003), Dust devils as observed by Mars Pathfinder, *J. Geophys. Res.*, *108*(E12), 5133, doi:10.1029/2000JE001421.
- Greeley, R., and S. D. Thompson (2003), Mars: Aeolian features and wind predictions at the Terra Meridiani and Isidis Planitia potential Mars Exploration Rover landing sites, *J. Geophys. Res.*, *108*(E12), 8093, doi:10.1029/2003JE002110.
- Greeley, R., R. Leach, B. White, J. Iversen, and J. Pollack (1980), Threshold windspeeds for sand on Mars: Wind tunnel simulations, *Geophys. Res. Lett.*, *7*, 121–124.
- Greeley, R., A. Skyeck, and J. B. Pollack (1993), Martian aeolian features and deposits: Comparisons with general circulation model results, *J. Geophys. Res.*, *98*(E2), 3183–3196.
- Greeley, R., S. C. R. Rafkin, R. M. Haberle, and R. O. Kuzmin (2001), Topography and aeolian features: Dunes and streaks compared with global and mesoscale wind predictions, *Lunar Planet. Sci.* [CD-ROM], XXXII, abstract 2003.
- Greeley, R., R. O. Kuzmin, S. C. R. Rafkin, T. I. Michaels, and R. Haberle (2003), Wind-related features in Gusev crater, Mars, *J. Geophys. Res.*, *108*(E12), 8077, doi:10.1029/2002JE002006.
- Hong, S.-Y., and H.-L. Pan (1996), Nonlocal boundary layer vertical diffusion in a medium-range forecast model, *Mon. Weather Rev.*, *124*, 2322–2339.
- Howard, A. D. (2000), The role of eolian processes in forming surface features of the Martian polar layered deposits, *Icarus*, *144*, 267–288.
- Iversen, J. D., and B. R. White (1982), Saltation threshold on Earth, Mars and Venus, *Sedimentology*, *29*, 111–119.
- Iversen, J. D., R. Greeley, J. B. Pollack, and B. R. White (1973), Simulation of Martian aeolian phenomena in the atmospheric wind tunnel, in *Proceedings of the 7th Conference on Space Simulation*, edited by R. T. Hollingsworth, *NASA Spec. Publ., NASA-SP 336*, 191–213.
- Iversen, J. D., J. B. Pollack, R. Greeley, and B. R. White (1976), Saltation threshold on Mars: the effect of interparticle force, surface roughness, and low atmospheric density, *Icarus*, *29*, 318–393.
- Joshi, M. M., R. M. Haberle, J. R. Barnes, J. R. Murphy, and J. Schaeffer (1997), Low-level jets in the NASA Ames Mars general circulation model, *J. Geophys. Res.*, *102*(E3), 6511–6523.
- Kuzmin, R. O., R. Greeley, S. C. R. Rafkin, and R. Haberle (2001), Wind-related modification of some small impact craters on Mars, *Icarus*, *153*, 61–70.
- Lee, P., and P. C. Thomas (1995), Longitudinal dunes on Mars: Relation to current with regimes, *J. Geophys. Res.*, *100*(E3), 5381–5395.
- Lindsay, J. F. (1973), Reversing barchan dunes in Lower Victoria Valley, Antarctica, *Geol. Soc. Am. Bull.*, *84*, 1799–1806.
- Liu, M., and D. L. Westphal (2001), A study of the sensitivity of simulated mineral dust production to model resolution, *J. Geophys. Res.*, *106*(D16), 18,099–18,122.
- Malin, M., and K. S. Edgett (2001), Mars Global Surveyor Mars Orbiter Camera: Interplanetary cruise through primary mission, *J. Geophys. Res.*, *106*(E10), 23,429–23,570.
- McCauley, J. F., M. H. Carr, J. A. Cutts, W. K. Hartmann, H. Masursky, D. J. Milton, R. P. Sharp, and D. E. Wilhelms (1972), Preliminary Mariner 9 report on the geology of Mars, *Icarus*, *17*, 289–327.
- McDonald, R. R., and R. S. Anderson (1995), Experimental verification of aeolian saltation and lee side deposition models, *Sedimentology*, *42*, 39–56.
- Newman, C. E., S. R. Lewis, P. L. Read, and F. Forget (2002), Modeling the Martian dust cycle, 1. Representations of dust transport processes, *J. Geophys. Res.*, *107*(E12), 5123, doi:10.1029/2002JE001910.
- Nickling, W. G., C. McKenna Neuman, and N. Lancaster (2002), Grainfall processes in the lee of transverse dunes, Silver Peak, Nevada, *Sedimentology*, *49*, 191–209.
- Paige, D. A., and K. D. Keegan (1994), Thermal and albedo mapping of the polar regions of Mars using Viking thermal mapper observations: 2. South polar region, *J. Geophys. Res.*, *99*(E12), 25,993–26,013.
- Paige, D. A., J. E. Bachman, and K. D. Keegan (1994), Thermal and albedo mapping of the polar regions of Mars using Viking thermal mapper observations: 1. North Polar region, *J. Geophys. Res.*, *99*(E12), 25,959–25,991.
- Palluconi, F. D., and H. H. Kieffer (1981), Thermal inertia mapping of Mars for 60°S to 60°N, *Icarus*, *45*, 415–426.
- Pleskot, L. K., and E. D. Miner (1981), Time variability of Martian bolometric albedo, *Icarus*, *45*, 179–201.
- Sagan, C., J. Veverka, P. Fox, L. Quam, R. Tucker, J. B. Pollack, and B. A. Smith (1972), Variable features on Mars: Preliminary Mariner 9 television results, *Icarus*, *17*, 346–372.
- Seguro, J. V., and T. W. Lambert (2000), Modern estimation of the parameters of the Weibull wind speed distribution for wind energy analysis, *J. Wind Eng. Ind. Aerodyn.*, *85*, 75–84.

- Sharp, R. P. (1963), Wind ripples, *J. Geol.*, *71*, 617–636.
- Sharp, R. P. (1966), Kelso Dunes, Mojave Desert, California, *Geol. Soc. Am. Bull.*, *77*, 1045–1074.
- Smith, D. E., et al. (2001), Mars Orbiter Laser Altimeter: Experiment summary after the first year of global mapping of Mars, *J. Geophys. Res.*, *106*(E10), 23,689–23,722.
- Smith, H. T. U. (1972), Aeolian deposition in Martian craters, *Nature Phys. Sci.*, *238*, 72–74.
- Toigo, A. D. (2001), Behavior of dust in the Martian atmosphere, Ph.D. thesis, 139 pp., Calif. Inst. of Technol., Pasadena.
- Toigo, A. D., and M. I. Richardson (2002), A mesoscale model for the Martian atmosphere, *J. Geophys. Res.*, *107*(E7), 5049, doi:10.1029/2000JE001489.
- Toigo, A. D., M. I. Richardson, R. J. Wilson, H. Wang, and A. P. Ingersoll (2002), A first look at dust lifting and dust storms near the south pole of Mars with a mesoscale model, *J. Geophys. Res.*, *107*(E7), 5050, doi:10.1029/2001JE001592.
- Toigo, A. D., M. I. Richardson, S. P. Ewald, P. J. Gierasch, and R. J. Wilson (2003), Numerical simulation of Martian dust devils, *J. Geophys. Res.*, *108*(E6), 5047, doi:10.1029/2002JE002002.
- Vasavada, A. R., J. Williams, D. A. Paige, K. E. Herkenhoff, N. T. Bridges, R. Greeley, B. C. Murray, D. S. Bass, and K. S. McBride (2000), Surface properties of Mars' polar layered deposits and polar landing sites, *J. Geophys. Res.*, *105*(E3), 6961–6970.
- White, B. R. (1979), Soil transport by winds on Mars, *J. Geophys. Res.*, *84*(B9), 4643–4651.
- Wilson, R. J., and K. Hamilton (1996), Comprehensive model simulation of thermal tides in the Martian atmosphere, *J. Atmos. Sci.*, *53*, 1290–1326.
- Wilson, S. A., and J. R. Zimbelman (2004), Latitude-dependent nature and physical characteristics of transverse aeolian ridges on Mars, *J. Geophys. Res.*, *109*, E10003, doi:10.1029/2004JE002247.

L. K. Fenton, Department of Geology, Arizona State University, Mail Code 1404, Tempe, AZ 85287, USA. (lkfenton@asu.edu)

M. I. Richardson, Division of Geological and Planetary Sciences, California Institute of Technology, MS 150-21, Pasadena, CA 91125, USA. (mir@gps.caltech.edu)

A. D. Toigo, Graduate School of Science and Technology, Kobe University, Rokkodai-cho 1-1, Nada-ku, Kobe 657-8501, Japan.